European Journal of
Mineralogy
Open Access

Trace and ultratrace elements in spinel subgroup minerals of ultramafic rocks from the Voltri Massif (NW Italy): the influence of microstructure and texture

Silvia Fornasaro[1], Paola Comodi[2], Laura Crispini[3], Sandro Zappatore[4], Azzurra Zucchini[2], and Pietro Marescotti[3]

[1]Dipartimento di Scienze della Terra, Università di Pisa, Via Santa Maria, 53, 56126, Pisa, Italy
[2]Dipartimento di Fisica e Geologia, Università di Perugia, Piazza dell'Università, 1, 06123, Perugia, Italy
[3]Dipartimento di Scienze della Terra, dell'Ambiente e della Vita, Università di Genova, Corso Europa, 26, 16132, Genoa, Italy
[4]Dipartimento di Ingegneria Navale, Elettrica, Elettronica e delle Telecomunicazioni, Università di Genova, Via alla Opera Pia 11A, 16145, Genoa, Italy

Correspondence: Silvia Fornasaro (silvia.fornasaro@unipi.it)

Abstract. An innovative multi-analytical approach comprising mineralogical, minero-chemical, and microstructural analyses as well as an indirect machine learning-based statistical method was applied to investigate the mineralogy and the mineral chemistry of spinel subgroup minerals (SSMs) of different ultramafic rocks from the high-pressure metaophiolites of the Voltri Massif (Central Liguria, NW Italy). The study was focused on the correlation between the compositional variations of SSMs and their texture, microstructure, and the degree of serpentinization of the host rock.

The SSM occurs with three main textures and microstructures linked to the progressive serpentinization and deformation of ultramafic rocks during the Alpine orogenic events: (i) Cr-spinel porphyroclasts with various degrees of recrystallization (up to magnetite porphyroblasts) within partially serpentinized peridotite and massive serpentinite; (ii) magnetite crystals associated with pseudomorphic and non-pseudomorphic serpentine textures (e.g., mesh, hourglass, ribbon, and interpenetrating textures) in partially serpentinized peridotite and massive serpentinites; and (iii) magnetite crystals re-oriented along the foliations developed in serpentine schist. The chemical composition of SSMs varies systematically within the textures and microstructures. These processes also affected the chemical composition of SSMs, the availability of Mn, Zn, Ni, and Co in solution, and their consequent incorporation in the lattice of chromian spinel due to olivine breakdown, the major repository of these elements in ultramafic rocks.

At a general scale, the trace and ultratrace variability is primarily related to the petrologic and tectonic evolution but, at a local scale, also the mineralogical, lithological, structural, and textural features correlated to the degree of serpentinization and/or deformation. These significantly influence the distribution and concentration of trace and ultratrace elements in SSMs. The results of the present work were also confirmed by an innovative indirect statistical method performed through the Weka Machine Learning Workbench.

1 Introduction

Spinels s.l. (sensu lato) are a very interesting class of minerals both for Earth and material sciences, since they crystallize in a wide range of physical–chemical conditions from crust to mantle on Earth as well as on extraterrestrial materials. Moreover, spinel-type structures have attracted interest in various research on solid-state physics for their peculiar characteristics.

The spinel-type structure is AB_2X_4, where A and B can be either a large number of different cations with a wide range of size and charge or vacancies that can be both accommodated in spinel given its flexible structure, and X are anions. According to Bosi et al. (2019), the 56 valid species of spinel are divided in three subgroups on the base of the X dominant: oxyspinel ($X = O^{2-}$), thiospinel ($X = S^{2-}$), and selenospinel ($X = Se^{2-}$) group.

Spinel subgroup minerals (SSMs hereafter) is a subgroup of the oxyspinel (the other subgroup in the oxyspinel is ulvöspinel) with divalent cations at the A site and trivalent cations at the B site.

SSMs occur in igneous, metamorphic, and sedimentary rocks, as well as in different types of ore deposits (Dupuis et al., 2011). These minerals form under a wide variety of genetic conditions ranging from primary crystallization in spinel-bearing mantle peridotites and sulfide melts to precipitation from relatively low-temperature (LT) hydrothermal fluids (Dare et al., 2014). They are also an important product of prograde and retrograde metamorphism of ultramafic rocks (Evans and Frost, 1975). In particular, the magnetite series forms in supergenic environments, as a pseudomorphic replacement after cassiterite, siderite, and sulfides, as well as in skarn (King, 2004). Finally, magnetite can also be produced by biologically induced mineralization (BIM) (Descamps et al., 2016). It represents a mineralogical species similar to amphiboles that crystallizes in a variety of environments and with which spinels can associate, whose crystallochemical flexibility can record the chemical and physical conditions of the formation environment and give important genetic information (e.g., water activity, oxygen fugacity; Comodi et al 2010).

SSMs can have a significant impact on the environment and human health since they may contain and, hence, they may be the source of potentially toxic elements (PTEs), which can be released into soils and circulating waters during weathering and pedogenesis. This process can be particularly significant in ultramafic soils, deriving from peridotites and serpentinites, which commonly have high concentration of PTEs, particularly Cr, Ni, and Co (e.g., Duivenvoorden et al., 2017; Romero-Freire et al., 2018; Fornasaro et al., 2019; Marescotti et al., 2019).

SSMs have a cubic closest packing structure (space group Fd-$3m$) with general formula XY_2O_4. The X site is occupied mainly by Mg^{2+} and Fe^{2+} in tetrahedral coordination, whereas the Y site is occupied by trivalent ions (mainly Fe^{3+}, Cr^{3+}, and Al^{3+}) in an octahedral coordination.

Several minor, trace, and ultratrace elements commonly substitute for either bivalent ions at the X site: Zn^{2+}, Co^{2+}, Mn^{2+}, and Ni^{2+}. The following applies for trivalent and tetravalent ions at the Y site: V^{3+}, Sc^{3+}, Ga^{3+}, and Ti^{4+} (Colás et al., 2014). However, others are known to occur in some specific SSMs, such as those in the magnetite series: Cu, Zr, Ba, As, Ge, Sn, Sc, Sr, Y, Nb, Mo, W, Hf, Ta, and Bi (Deditius et al., 2018).

The chemical composition of SSMs may vary considerably in response to the various genetic processes involved in their formation, and for this reason they have been often used as efficient fingerprints to discriminate mantle melting processes and tectonic settings, as well as to reconstruct the metamorphic and metasomatic evolution of their host rocks (e.g., Irvine, 1967; Barnes and Roeder, 2001; Rollinson, 2008; Nadoll et al., 2014). The chemical composition of SSMs has been also used in discriminating different mineralizing systems in ore deposits as well as in establishing the nature of sedimentary source areas in foreland basins (e.g., Abre et al., 2009; Pagè and Barnes, 2009; Chen et al., 2020).

In this contribution we analyze possible correlations between the compositional variations of SSMs with the textures, microstructures, and the degree of serpentinization of ultramafic rocks from meta-ophiolitic rocks of the Voltri Massif (Ligurian Alps, NW Italy). SSMs occur in partially serpentinized peridotites, massive antigorite serpentinites, and foliated antigorite serpentinites and were investigated using a multi-analytical approach comprising mineralogical and microstructural analysis, scanning electron microscopy and microanalysis (SEM-EDS and EMPA), and in situ measurements of trace and ultratrace elements by laser ablation inductively coupled plasma mass spectrometry (LA-ICP-MS). The possible correlations between the compositional variations of SSMs with the type of rock and/or microstructure were also evaluated through an indirect statistical method as implemented in the machine learning software Weka 3.8.0 (Frank et al., 2016).

2 Geological setting

The study area is located in the NW part of the Voltri Massif (VM), a wide metamorphic ophiolite body (about $800\,\mathrm{km^2}$) at the southernmost termination of the Western Alps (Ligurian Alps, NW Italy; Fig. 1).

The VM represents a remnant of the Jurassic Ligurian Tethys and is composed of tectono-metamorphic units accreted during the Alpine orogenesis (Capponi et al., 2016, and references therein). These units consist mainly of mafic to ultramafic rocks derived from different paleogeographic domains, including subcontinental mantle, oceanic lithosphere with sedimentary covers, and subordinate continental crust. The units of the VM show a polyphase tectono-

metamorphic evolution with blueschist to eclogite facies peak metamorphism and variable retrogressive overprints down to the greenschist facies conditions (e.g., Messiga et al., 1983; Capponi et al., 2016; Scarsi et al., 2018).

In the VM, peridotites occur as kilometer-scale bodies and consist mainly of spinel- and plagioclase-bearing lherzolite, with minor harzburgite, dunite lenses, and pyroxenite bands. They are affected by various degrees of serpentinization developed mainly along networks of anastomosing shear zones separating domains of low-deformed to undeformed peridotites (Scambelluri et al., 1991; Cannaò et al., 2016). The study area comprises partially serpentinized peridotites and antigorite serpentinites (Fig. 1c).

Antigorite serpentinites comprise both antigorite-bearing massive serpentinites and antigorite-bearing serpentine schists, occasionally with textural relics of the mantle peridotites. They represent the most abundant lithotype of the VM, cropping out over a total area of more than $200 \, \text{km}^2$. Gradual transitions from massive and essentially undeformed serpentinites to strongly foliated serpentine schist occur over the entire study area. Serpentine schists are commonly characterized by a pervasive composite schistosity, with multiple folding phases and shear bands (Scambelluri et al., 1991; Federico et al., 2015; Capponi et al., 2016, and references therein).

3 Materials and methods

Forty-five samples of ultramafic rocks were collected from eight sites of the VM (Fig. 1c), selected according to the degree of serpentinization as well as to textural and structural criteria (e.g., intensity of foliation, degree of fracturing, presence of shear zones or tectonic contacts with other lithologies). Based on field investigations and on mineralogical, petrographic, and micro-structural/textural analyses, three main groups of ultramafic rocks were distinguished (15 samples for each group): (i) partially serpentinized peridotites, (ii) massive serpentinites, and (iii) foliated serpentinites. The mineralogy, mineral chemistry, petrography, and bulk chemistry of the three groups were previously investigated and are reported in Fornasaro et al. (2019).

In the present work SSMs were analyzed using a multi-scale and multi-analytical approach including the following: (i) micro-structural/textural analyses by means of polarized-light optical microscopy (PLOM), (ii) major and minor elements analysis using an electron microprobe analyzer (EMPA-WDS), and (iii) in situ measurements of trace and ultratrace elements by laser ablation inductively coupled plasma mass spectrometry (LA-ICP-MS).

The micro-structural/textural investigations were carried out at the DISTAV Department, University of Genoa (Italy), using the BX-41 Olympus Microscope equipped with $2\times$, $4\times$, $10\times$, $20\times$, $40\times$, and $50\times$ objective magnifications and $10\times$ and $12.5\times$ eyepieces.

Major (i.e., Mg, Al, Cr, and Fe) and minor (i.e., Ti, V, Mn, Zn, Si, Co, K, Ca, and Ni) elements in SSMs were analyzed using the EMPA-WDS JEOL 8200 Super Probe at the "Ardito Desio" Department of Earth Sciences, University of Milan (Italy). The analytical conditions were set at 15 kV accelerating voltage, 4.9 nA beam current, and a counting time of 20 s on the peaks and 10 s on the background. Beam diameter is 1 μm. Calibration for chemical analysis was accomplished using the following standards: olivine (Mg), omphacite (Na), Cr_2O_3 (Cr), rhodonite (Mn and Zn), K-feldspar (K), anorthite (Al and Ca), wollastonite (Si), metallic vanadium (V), fayalite (Fe), ilmenite (Ti), cobalt oxide (Co), galena (S), and niccolite (Ni). Raw element data were ZAF-corrected using a phi–rho–Z analysis program, and corrected element contents were converted to oxide contents in weight percent (wt %) assuming stoichiometry. Detection limit is approximately 330 ppm for Ti (6 % standard deviation), 460 ppm for Mn (6 % standard deviation), 160 ppm for Mg (2 % standard deviation), 180 ppm for Si (6 % standard deviation), 320 ppm for V (12 % standard deviation), 370 ppm for Fe (8 % standard deviation), 140 ppm for Ca (15 % standard deviation), 135 ppm for Al (4 % standard deviation), 370 ppm for Cr (10 % standard deviation), 390 ppm for Ni (9 %standard deviation), and 800 ppm for Zn (9 % standard deviation). FeO represents total iron (oxide) content. Detailed compositional X-ray intensity maps were obtained for selected areas to investigate the distribution of major and minor elements (i.e., Cr, Fe, Mg, Mn, Ni, S, and Si) in SSMs. The analytical conditions for image acquisition were 15 kV accelerating voltage, $1 \, \mu\text{m}^2$ pixel size, and a 30 ms dwell time.

In situ quantitative analyses of major, minor, trace, and ultratrace elements (Al, Ca, Co, Cr, Cu, K, Mg, Mn, Na, Ni, Si, Ti, V, Zn, Ba, Cs, Ga, Hf, Li, Nb, P, Pb, Rb, Sc, Sn, Sr, Ta, Th, U, Y, and Zr) were determined using a Thermo Fisher Scientific iCAP Q quadrupole mass spectrometer coupled with a Teledyne/Photon Machine ArF Excimer G2 laser ablation system of laboratory of Petro-Volcanology Research Group at Department of Physics and Geology, University of Perugia, Italy. The analyses were conducted using a ~ 30–$20 \, \mu\text{m}$ beam diameter, 8 Hz frequency, and 0.032–0.105 mJ pulse power, during the 90 s analysis (50 s for the gas blank and 40 s on the grain). Details on the working conditions, instrumentation, precision, and accuracy are reported in Petrelli et al. (2016).

The structural formula of SSMs was calculated assuming stoichiometry, following the procedure of Droop (1987); these minerals were classified according to Gargiulo et al. (2013).

The statistical evaluation of the possible correlations between the compositional variation in SSMs and the rock type and/or microstructures was performed by means of Weka 3.8.0 (Frank et al., 2016), a machine learning software package written in Java and freely downloadable from
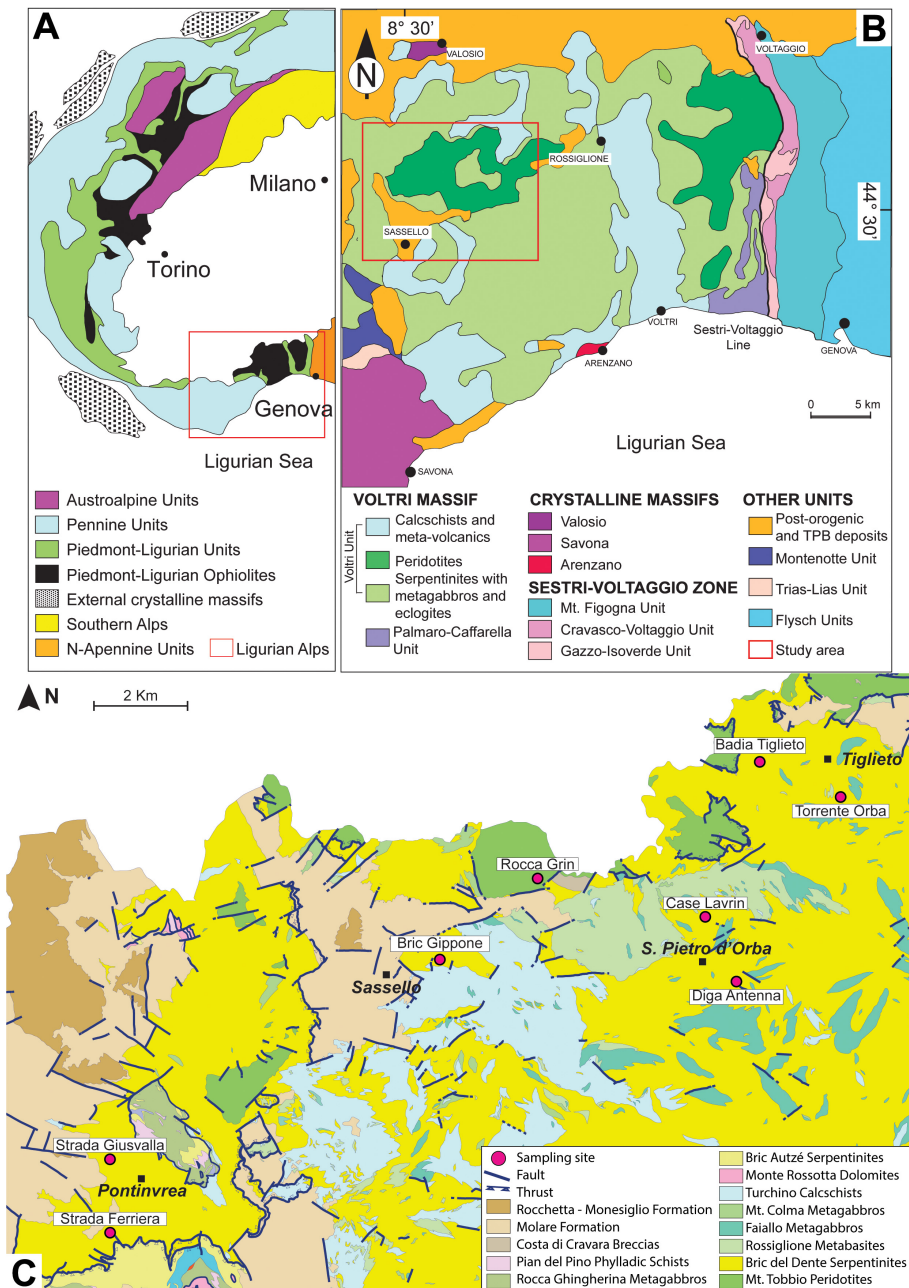
Figure 1. (a) Sketch map of the Western Alps. **(b)** Geological map of the Voltri Massif and adjoining units, modified after Capponi and Crispini (2002). **(c)** Geological map of the study area with the sampling site location (red dots), modified after Capponi et al. (2013).

https://sourceforge.net/projects/weka/ (last access: 20 February 2023).

4 Results

4.1 Classification of the VM spinel subgroup

The composition of SSMs occurring in the three groups of rocks is shown in Table 1 and Fig. 2. SSMs classified accord-ing to the chemical substitution at the Y site (Fig. 2a) have a wide compositional range covering the fields of Cr-spinel, ferrian chromite, Cr-magnetite, and magnetite (Fig. 2). Us-ing the classification according to the chemical substitution at the X site (Fig. 2b), most of the SSMs are in the magnetite field, whereas only some SSMs in the partially serpentinized peridotites fall into the pleonaste field.

SSM minerals in the studied rocks are mainly (Fig. 2c–d) the following:

i. Cr-spinel with Fe# = [Fe^{3+} / (Fe^{3+}+Fe^{2+})] = 0.1–0.22, Mg# = [Mg / (Mg + Fe^{2+})] = 0.3–0.7, Cr# = [Cr / (Cr + Al)] = 0.2–0.4, in partially serpentinized peridotites;

ii. rare ferrian chromite with Fe# = 0.4–0.6, Mg# = 0.15–0.2, Cr# = 0.75–0.9, in partially serpentinized peridotites;

iii. Cr-magnetite with Fe# = 0.4–0.68, Mg# = 0.01–0.2, Cr# = 0.7–0.97, and Fe# = 0.5–0.68, Mg# = 0–0.2, Cr# = 0.9–1, for porphyroclasts in partially serpentinized peridotites and massive serpentinites, respectively;

iv. magnetite with Fe# = 0.68–0.69, Mg# = 0.01–0.02, and a significant amount of Cr (i.e., Cr# = 0.27–0.38).

4.2 Microstructure and texture of the VM spinel subgroup

In the three rock groups, SSMs have been grouped in the following classes (Fig. 3), according to their different microstructures and textures.

4.2.1 SSM porphyroclasts

The porphyroclasts mainly consist of scattered sub-euhedral crystals, varying in size between 0.1 and 2 mm. They show various degrees of recrystallization, evolving from pristine mantle spinels.

Primary mantle spinels porphyroclasts are Cr-spinels and are found in partially serpentinized peridotites; these porphyroclasts mainly occur with an amoeboid or holly leaf morphology (e.g., Fig. 3a–b), in which Cr-spinel is surrounded by Cr-chlorite coronas that have a content of Cr up to 5900 ppm. Replacement of Cr-spinel by ferrian chromite / Cr-magnetite spongy rims starts along rims and fractures and progressively affects the Cr-spinel.

In the massive serpentinites, porphyroclasts are mainly represented by Cr-magnetite relics at the core with rims having a magnetite composition; this substitution is visible also along microfractures and veins cutting porphyroclasts (Fig. 3c–d).

In the foliated serpentinites, pseudomorphs of almost "pure" magnetite after Cr-magnetite occur along the foliation.

4.2.2 Idiomorphic to sub-idiomorphic SSMs

Idiomorphic to sub-idiomorphic SSMs (10 to 40 µm in size) occur in trails within the different pseudomorphic serpentinite textures: (i) bastites texture, with very fine magnetite arranged along the cleavage planes of clinopyroxenes and orthopyroxenes (mainly augite, diopside, and enstatite) (Fig. 3e) or (ii) along the rims of the mesh, hourglass, and ribbon textures of former olivines, regardless of the degree of serpentinization of the rock (i.e., partially serpentinized peridotites vs. massive serpentinites) (Fig. 3f).

In non-pseudomorphic serpentinites spinels may occur as sub-millimeter scattered crystals. In general, all these SSMs have magnetite composition (e.g., Fe# = 0.68–0.69, Mg# = 0.01–0.02, Cr# = 0.27–0.38).

4.2.3 SSM porphyroclasts along foliation and shear zones

In foliated serpentinites and in millimeter-thick shear zones cutting massive serpentinites, SSMs occur either as aggregates of allotriomorphic crystals (60 to 130 µm) or as micrometer-size crystals, oriented along the folded composite fabric (Fig. 3g–h). All these crystals are classifiable as magnetite, but substantial compositional differences exist depending on the degree of serpentinization and deformation experienced by the host rock. For example, magnetite found within the shear zones of massive serpentinites has a higher Mg and lower Cr content than that found in foliated serpentinites.

4.3 Crystal chemistry and trace and ultratrace elements of SSMs

The analysis of trace and ultratrace elements in SSMs highlighted that their most important carrier in the studied rocks is porphyroclasts.

In general, the contents of Mg (Fig. 2d), Al, V, Cr, and Zn (Figs. 4–5) are higher in the porphyroclasts of partially serpentinized peridotites than those of massive serpentinites and foliated serpentinites. Conversely, the contents of Ni, Co, and Mn increase from porphyroclasts of partially serpentinized peridotites to those of massive serpentinites (Fig. 4). Nevertheless, porphyroclasts in massive serpentinites are richer in Ni and Mn than those occurring in foliated serpentinites (see enlarged area in the Fig. 4a and c).

In mesh-hosted magnetites, significant amounts of Ni (∼ 0.03 apfu) and Co (∼ 0.008 apfu) occur, whereas bastite-hosted magnetites have a significant amount of Cr (∼ 0.05 apfu), regardless of the rock in which they occur.

Re-oriented magnetites, in shear zones cutting massive serpentinites, contain more Mg (∼ 0.05 apfu; not show in the figures), Ni (∼ 0.02 apfu), and Mn (∼ 0.014 apfu) compared to spinels in foliated serpentinites. On the other hand, foliated serpentinite SSMs (mainly magnetites) host a higher content of Cr (∼ 0.08 apfu) and Ti (∼ 0.01 apfu) compared to SSMs in shear zones cutting massive serpentinites. Moreover, the analytical results (Fig. 6) highlight different correlation among trace elements. Manganese (Fig. 6a) has a good positive correlation with Cr in all the rock types and in particular in the re-oriented crystals occurring in massive and foliated serpentinites (see enlarged area of Fig. 6a). Vanadium, Zn, and Ti (Fig. 6b–d) have positive correlation with
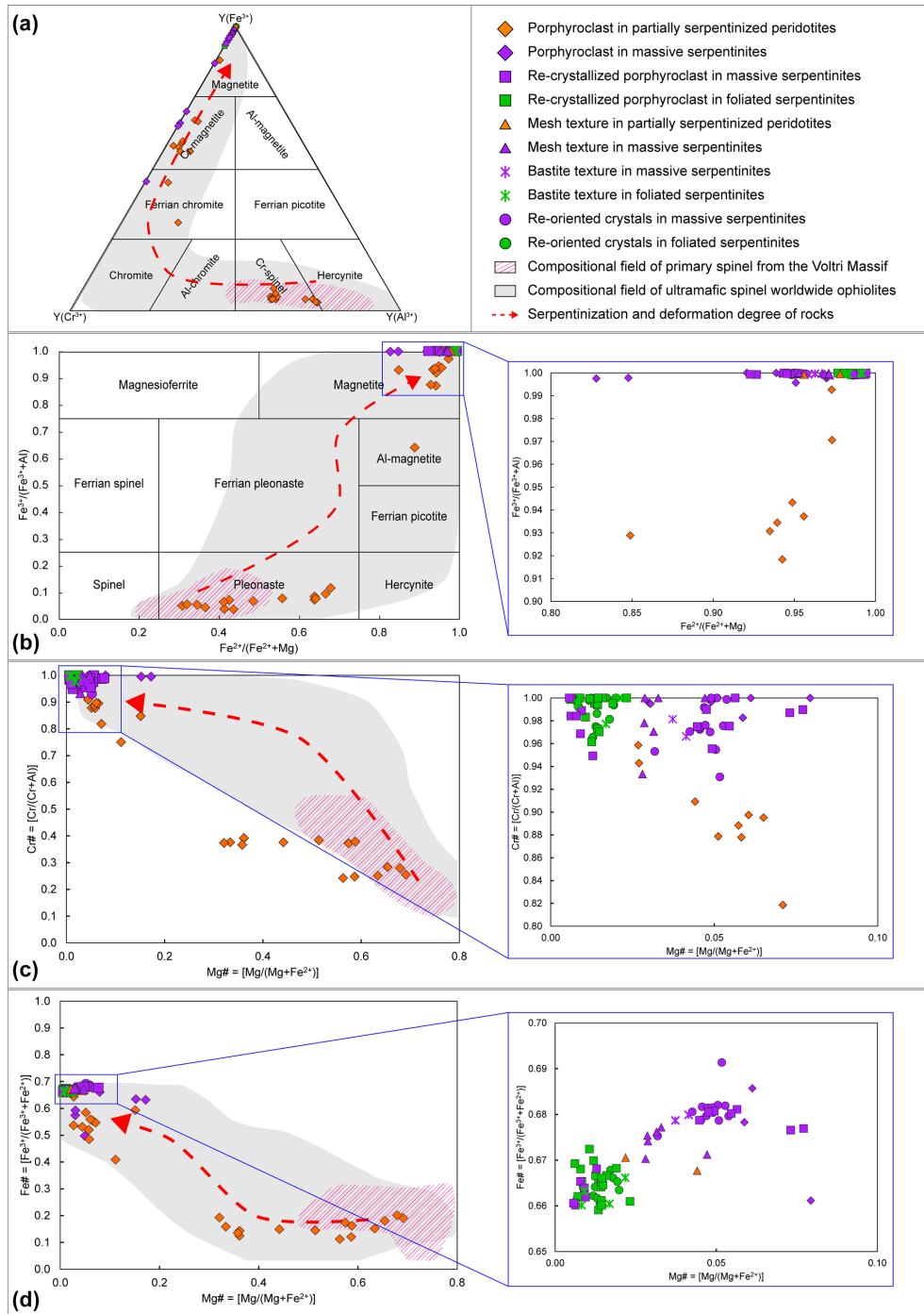
Figure 2. Classification diagrams of spinel subgroup minerals; SSMs are grouped according to their microstructure and texture; dashed pink areas refer to the composition of primary spinel from the Voltri Massif (mainly Erro-Tobbio primary spinels; Rampone et al., 2005; Piccardo and Visser, 2007; Borghini et al., 2007; Padovano et al., 2015); gray fields refer to the composition of ultramafic spinel in worldwide ophiolites (see Barnes and Roeder, 2001, and references therein). **(a)** Ternary diagram considering the Al^{3+}, Cr^{3+}, and Fe^{3+} exchange at the Y structural site (field contours are from Gargiulo et al., 2013). **(b)** Binary diagram considering the Mg^{2+}–Fe^{2+} exchange at the X structural site (field contours are from Gargiulo et al., 2013). **(c)** Mg# $= [Mg / (Mg + Fe^{2+})]$ vs. Cr# $= [Cr / (Cr + Al)]$ diagram of spinel subgroup minerals. **(d)** Mg# $= [Mg / (Mg + Fe^{2+})]$ vs. Fe# $= [Fe^{3+} / (Fe^{3+} + Fe^{2+})]$ diagram of spinel subgroup minerals. In the blue boxes the enlarged areas of panels **(b)**, **(c)**, and **(d)** are shown.

Table 1. Representative analysis of SSMs, chosen to acquire a representative selection of the different rocks and textures (formula calculated based on four cations) (bdl – below detection limits).

| Rock	Partially serpentinized peridotites					Massive serpentinites							Foliated serpentinites		
Microstructure	Cr-spinel	Porphyroclast	Porphyroclast		Mesh texture	Porphyroclast	Porphyroclast		Re-crystallized porphyroclast	Bastite texture	Mesh texture	Re-oriented crystal	Re-crystallized porphyroclast	Bastites texture	Re-oriented crystal
Minerals	Cr-spinel	Ferrian chromite	Cr-magnetite	Magnetite	Magnetite	Ferrian chromite	Cr-magnetite	Magnetite	Magnetite	Magnetite	Magnetite	Magnetite	Magnetite	Magnetite	Magnetite
SiO$_2$	0.06	0.07	0.84	0.08	0.69	0.02	0.08	bdl	0.02	0.02	0.02	0.09	0.09	0.03	0.09
TiO$_2$	0.12	0.42	0.25	0.14	0.01	0.62	0.70	0.27	0.18	0.13	0.07	0.06	0.12	0.61	0.21
Al$_2$O$_3$	44.03	8.12	2.31	0.29	0.03	0.09	0.06	bdl	0.03	0.03	bdl	0.04	0.04	0.02	0.01
Cr$_2$O$_3$	22.02	36.37	19.22	7.21	0.02	36.20	22.61	8.80	1.59	1.12	0.84	0.76	1.58	1.53	1.68
FeO	18.61	49.63	71.67	86.73	91.38	57.37	70.26	83.64	92.37	90.11	90.69	91.26	91.51	91.55	92.47
MgO	15.33	2.06	2.91	0.48	0.79	0.83	0.52	1.37	0.16	0.70	0.56	0.86	0.22	0.30	0.34
MnO	0.14	0.45	0.24	0.06	0.12	1.66	1.11	0.69	0.15	0.40	0.32	0.38	0.19	0.12	0.18
NiO	0.15	0.26	0.39	0.43	0.11	0.18	0.30	0.81	0.39	0.62	0.63	0.73	0.55	0.38	0.34
CaO	0.01	bdl	0.01	bdl	0.01	bdl	0.01	bdl	bdl	0.01	bdl	0.16	bdl	0.02	0.01
Na$_2$O	bdl	0.05	0.02	0.02	bdl	0.01	0.01	bdl	0.01	0.04	0.02	0.21	bdl	bdl	bdl
K$_2$O	bdl	bdl	bdl	0.002	bdl	0.01	bdl	0.003	0.01	bdl	bdl	bdl	0.001	bdl	bdl
V$_2$O$_5$	0.12	0.29	0.26	0.20	bdl	0.14	0.16	0.06	0.11	0.05	0.06	0.10	0.05	0.05	0.03
CoO	0.04	0.08	0.03	0.14	0.14	0.21	0.12	0.11	0.13	0.24	0.13	0.19	0.10	0.14	0.15
ZnO	0.13	0.79	0.07	0.07	0.06	0.57	0.35	0.09	bdl	bdl	bdl	0.12	0.16	0.03	bdl
Sum	100.77	98.57	98.23	95.85	93.36	97.92	96.30	95.85	95.16	93.47	93.34	94.97	94.60	94.79	95.49
Si	0.002	0.002	0.030	0.003	0.026	0.001	0.003	–	0.001	0.001	0.001	0.003	0.003	0.001	0.003
Ti	0.003	0.011	0.007	0.004	0.000	0.017	0.020	0.007	0.005	0.004	0.002	0.002	0.004	0.017	0.006
Al	1.437	0.339	0.097	0.013	0.001	0.004	0.003	–	0.002	0.001	–	0.002	0.002	0.001	0.0003
Cr	0.482	1.017	0.542	0.213	0.001	1.064	0.672	0.259	0.047	0.034	0.025	0.023	0.047	0.046	0.050
Mg	0.633	0.109	0.155	0.027	0.045	0.046	0.029	0.076	0.009	0.040	0.032	0.048	0.012	0.017	0.019
Mn	0.003	0.014	0.007	0.002	0.004	0.052	0.035	0.022	0.005	0.013	0.010	0.012	0.006	0.004	0.006
Ni	0.003	0.007	0.011	0.013	0.004	0.005	0.009	0.024	0.012	0.019	0.019	0.022	0.017	0.012	0.010
Ca	0.0004	–	0.0005	0.001	0.0003	–	0.001	–	–	0.001	0.001	0.006	–	0.001	0.0003
Na	–	0.003	0.001	0.001	–	0.001	0.001	0.0002	0.001	0.003	0.001	0.015	0.00003	–	0.0003
K	–	–	0.0001	0.0001	–	0.001	0.001	0.002	0.001	–	–	–	0.001	–	–
V	0.002	0.007	0.006	0.005	0.004	0.004	0.004	0.003	0.003	0.001	0.001	0.002	0.001	0.001	0.001
Co	0.001	0.002	0.001	0.004	0.002	0.006	0.004	0.003	0.004	0.007	0.004	0.006	0.003	0.004	0.005
Zn	0.003	0.021	0.002	0.002	0.002	0.016	0.010	0.003	–	0.001	–	0.003	0.004	0.001	–
Fe^{3+}	0.066	0.600	1.269	1.746	1.945	0.887	1.269	1.722	1.933	1.956	1.966	1.974	1.933	1.912	1.930
Fe^{2+}	0.365	0.868	0.870	0.967	0.968	0.897	0.941	0.882	0.979	0.921	0.937	0.881	0.967	0.983	0.971
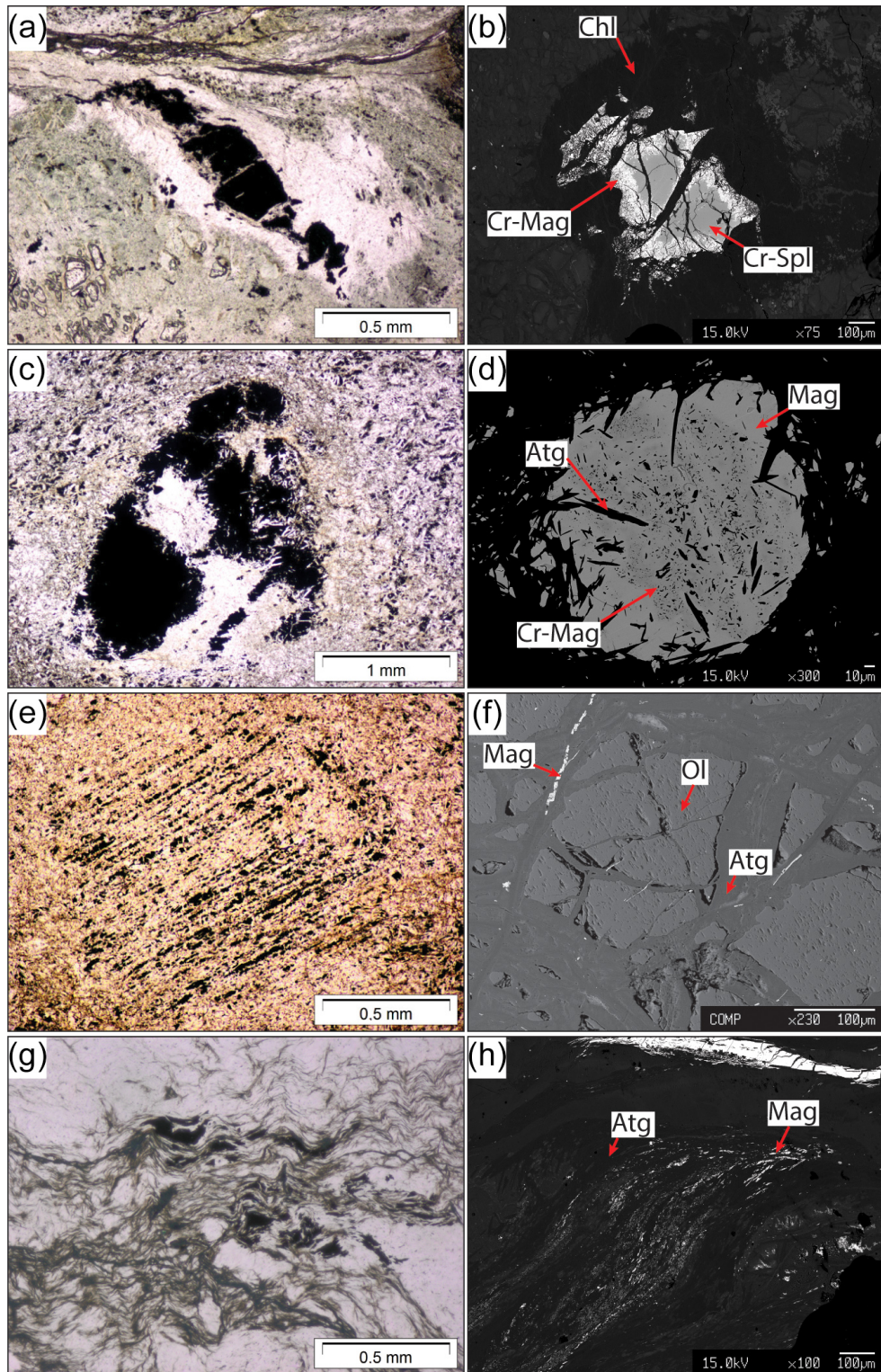
Figure 3. Spinel subgroup mineral microstructures: **(a–b)** SSM porphyroclasts surrounded by chlorite coronas, in partially serpentinized peridotites; **(c–d)** recrystallized SSM porphyroclasts intergrowing with serpentine minerals in massive serpentinites; **(e)** SSMs within bastite in massive serpentinites; **(f)** SSMs within mesh texture in partially serpentinized peridotites; **(g–h)** SSMs re-oriented along the foliation in foliated serpentinites. Mineral abbreviations from Warr (2021): Chl – chlorite, Cr-Mag – chromian magnetite, Cr-Spl – chromian spinel, Atg – antigorite, Mag – magnetite, Ol – olivine. Panels **(a)**, **(c)**, **(e)**, and **(g)** are petrographic microscope microphotographs with plane-light; panels **(b)**, **(d)**, **(f)**, and **(h)** are backscattered electron (BSE) images.
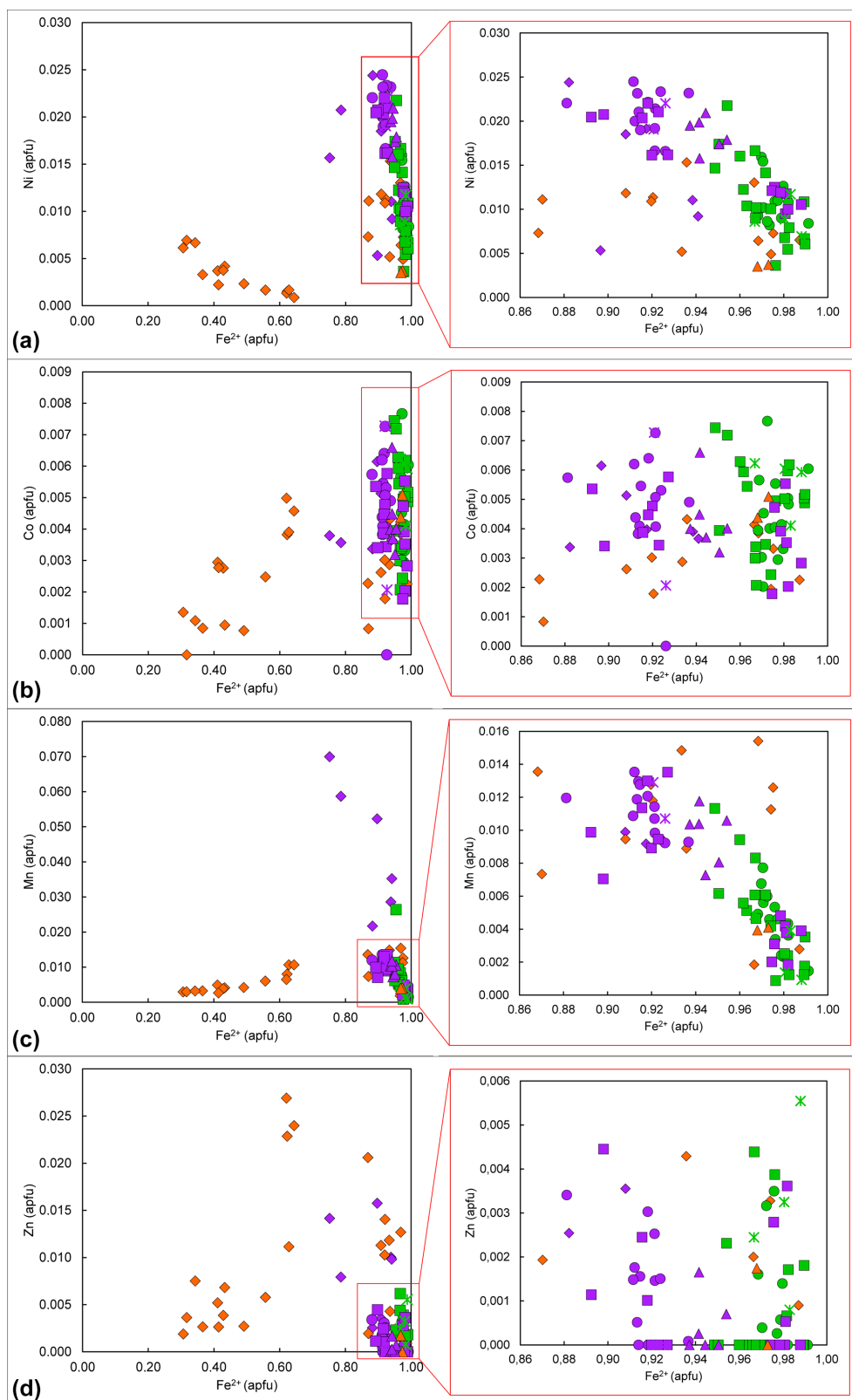
Figure 4. Correlation plots of Fe^{2+} (structural site X) vs. Ni **(a)**, Co **(b)**, Mn **(c)**, and Zn **(d)**. Values are in atoms per formula unit (apfu). Diagrams on the right are the zoomed area of the left diagram (red box) reported only for SSMs within serpentine textures and re-oriented along the foliation. For the legend of symbols please refer to Fig. 2.
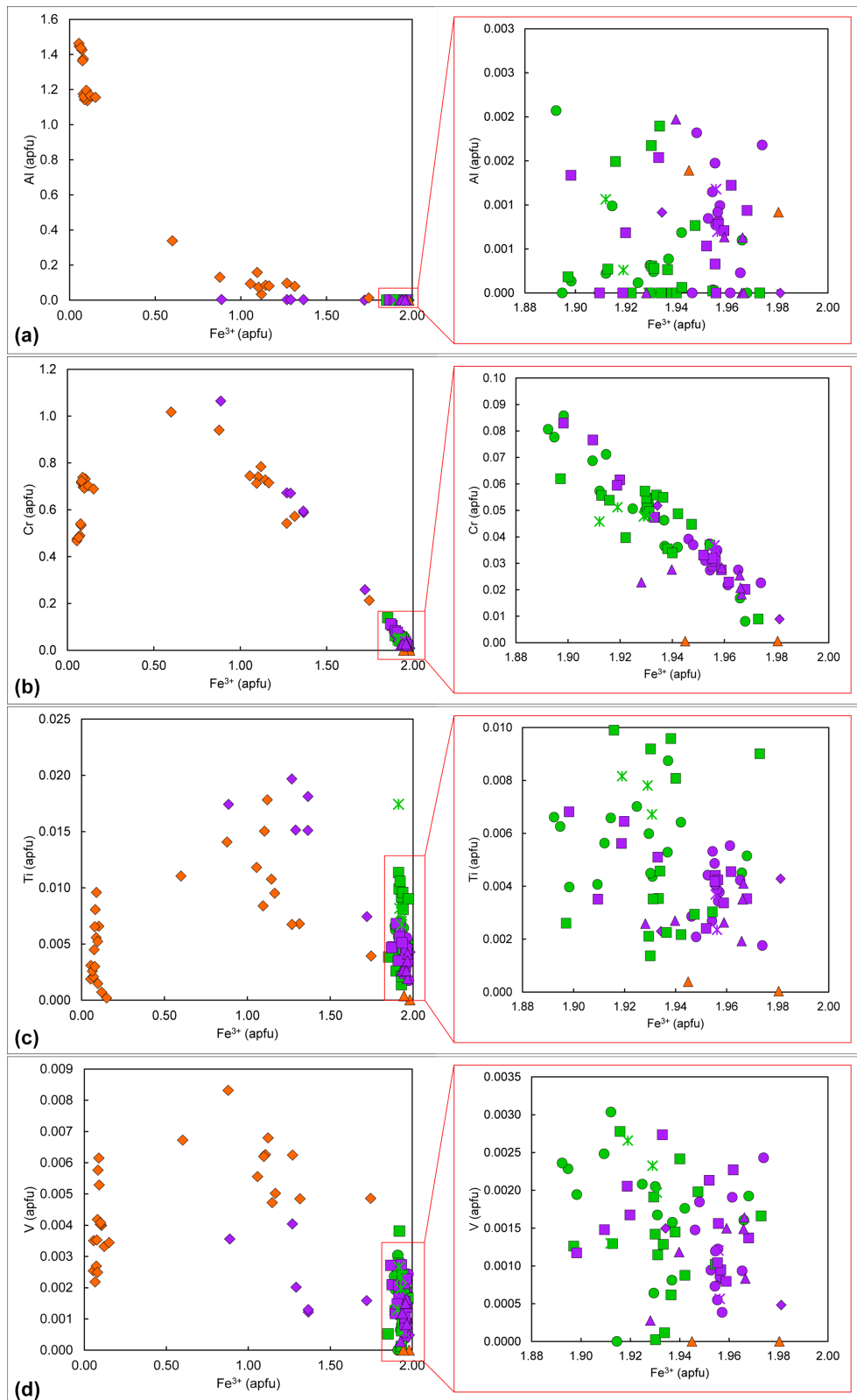
Figure 5. Correlation plots of Fe^{3+} (structural site Y) vs. Al (**a**), Cr (**b**), Ti (**c**), and V (**d**). Values are in atoms per formula unit (apfu). Diagrams on the right are the zoomed area of the left diagram (red box) reported only for SSMs within serpentine textures and re-oriented along the foliation. For the legend of symbols please refer to Fig. 2.

Cr mainly in porphyroclasts of partially serpentinized peridotites and massive serpentinites. Nickel shows positive correlation both in porphyroclast of massive serpentinites and in the re-oriented crystals in massive and foliated serpentinites (see enlarged area of Fig. 6e). Cobalt does not show a clear correlation with Cr (Fig. 6f).

Figure 7 provides an overview of the concentration of a wide range of elements within SSMs and shows high contents of Cr, Ni, V, Co, Ti, Mn, Zn, Sn, Pb, and Ga, which are compatible in magnetite, and low Zr, Hf, Sc, Ta, and Nb values, which are incompatible in magnetite (Dare et al., 2014).

5 Discussion

The chemistry and microstructure of SSMs in ultramafic rocks can be significantly modified both during oceanic serpentinization and/or prograde and retrograde metamorphism (Barnes, 1998, 2000). SSMs occurring in the studied rocks have similar chemical characteristics as those described by Evans and Frost (1975), Barnes and Roeder (2001), and Gargiulo et al. (2013) for SSMs related to metamorphosed ultramafic rocks from alpine-type complexes (Fig. 2). The analyzed SSMs record various stages of evolution linked to the multiphase geological history of the VM (Fig. 8). In the following, we will describe and discuss the effects of serpentinization and deformation on texture, microstructure, and chemistry of the studied SSMs. A possible evolution of the SSM microstructures is sketched in Fig. 8.

5.1 Texture and microstructure of SSMs

In VM, the partially serpentinized peridotites show preserved pseudomorphic textures of serpentine (mainly mesh texture and bastite) linked to the early stage of oceanic serpentinization of the lithospheric mantle. In these textures magnetite microcrystals occur either within the mesh rims or along cleavage planes of bastites.

Cr-spinels were altered by oceanic hydrothermal fluids that promoted the reaction with silicates (i.e., olivine and pyroxene), forming rims and veins of ferrian chromite and/or Cr-magnetite, and Cr-chlorite coronas (Cr-clinochlore), at a temperature likely higher than 200–300 °C (e.g., Grieco and Merlini, 2012; Merlini et al., 2012). After this reaction, olivine and spinel were residually enriched respectively in Fe^{2+} and Cr by a loss of MgO (olivine) and Al_2O_3 (spinel) (Piccardo et al., 2001; Colás et al., 2014).

The compositional map (Fig. 9) of spinel porphyroclasts shows that they were depleted in Cr and other metals starting from veins, as already observed for serpentinization processes (see Barnes, 2000). Therefore, the spongy alteration texture of the spinel rims and the sites close to cracks of the Cr-spinel can be attributed to the dissolution of several elements (i.e., Al, Cr, Ti, Mg, Zn, and Co) from these crystals during the serpentinization processes as also reported by other authors (e.g., Garuti et al., 2007; Teixeira et al., 2012). The reactions producing ferrian chromite and Cr-clinochlore have already been assessed in several studies (e.g., Christofides et al., 1994; Barnes and Roeder, 2001; Piccardo et al., 2001; Grieco and Merlini, 2012; Colás et al., 2014); however, there is no general agreement on the timing of this reactions, suggesting different processes such as (i) a pre-oceanic serpentinization process, but after all deep magmatic events (Grieco and Merlini, 2012; Merlini et al., 2012), (ii) during the oceanic serpentinization process (Bliss and MacLean, 1975), (iii) after the serpentinization of the rock (Kimball, 1990; Mellini et al., 2005), during prograde metamorphism of serpentinized ultramafic rocks (Evans and Frost, 1975; Barnes and Roeder, 2001), during the retrograde evolution from the high-pressure (HP) conditions (Gervilla et al., 2012; Colás et al., 2014), or during regional metamorphism of ultramafic rocks, after the reactions of spinel with silicates and metamorphic fluids (Barnes and Roeder, 2001).

According to what was observed in massive serpentinites from VM, we suggest that, during the ongoing oceanic serpentinization of the mantle rocks (Fig. 8, Stage B–C), mantle spinel (see dashed pink areas in Figs. 2 and 6 for the composition) was progressively replaced by magnetite, as attested by the occurrence of Cr-rich core relics, surrounded by Cr-poor magnetite rims (Diella et al., 1994; Fontana et al., 2008). With the progressive increase of serpentinization degree, mesh texture evolved to hourglass texture and then, at the early stage of deformation, to ribbon texture.

The progressive evolution, affecting the partially serpentinized peridotites during the $HP–LT$ subduction and exhumation events (e.g., Scambelluri et 2001; Peters et al., 2020), caused recrystallization and the almost complete obliteration of the oceanic pseudomorphic textures with the subsequent formation of non-pseudomorphic massive or foliated serpentinites. During these events, the formation of magnetite porphyroblasts and the grain-size reduction of recrystallized magnetite porphyroclasts occurred in massive serpentinite (Fig. 8, Stage D1). In foliated serpentinites, magnetite micrometer-sized crystals were re-oriented in trails along the main foliation (Fig. 8, Stage D2).

5.2 Chemical variation in spinel subgroup minerals

The obtained results provide evidence that the wide compositional variations in trace and ultratrace elements of SSMs are mainly controlled by the degree of serpentinization and tectonic deformation.

In general, the trace and ultratrace element content of SSMs seems to be mostly affected by the olivine breakdown during serpentinization (Barnes and Roeder, 2001; Gahlan and Arai, 2007). In the studied rocks, olivines contain high concentrations of Ni (up to 3514 ppm), Co (up to 661 ppm), Mn (up to 1795), and Zn (up to 1221 ppm) (Fornasaro et al., 2019) and can be considered the main repository of these elements.
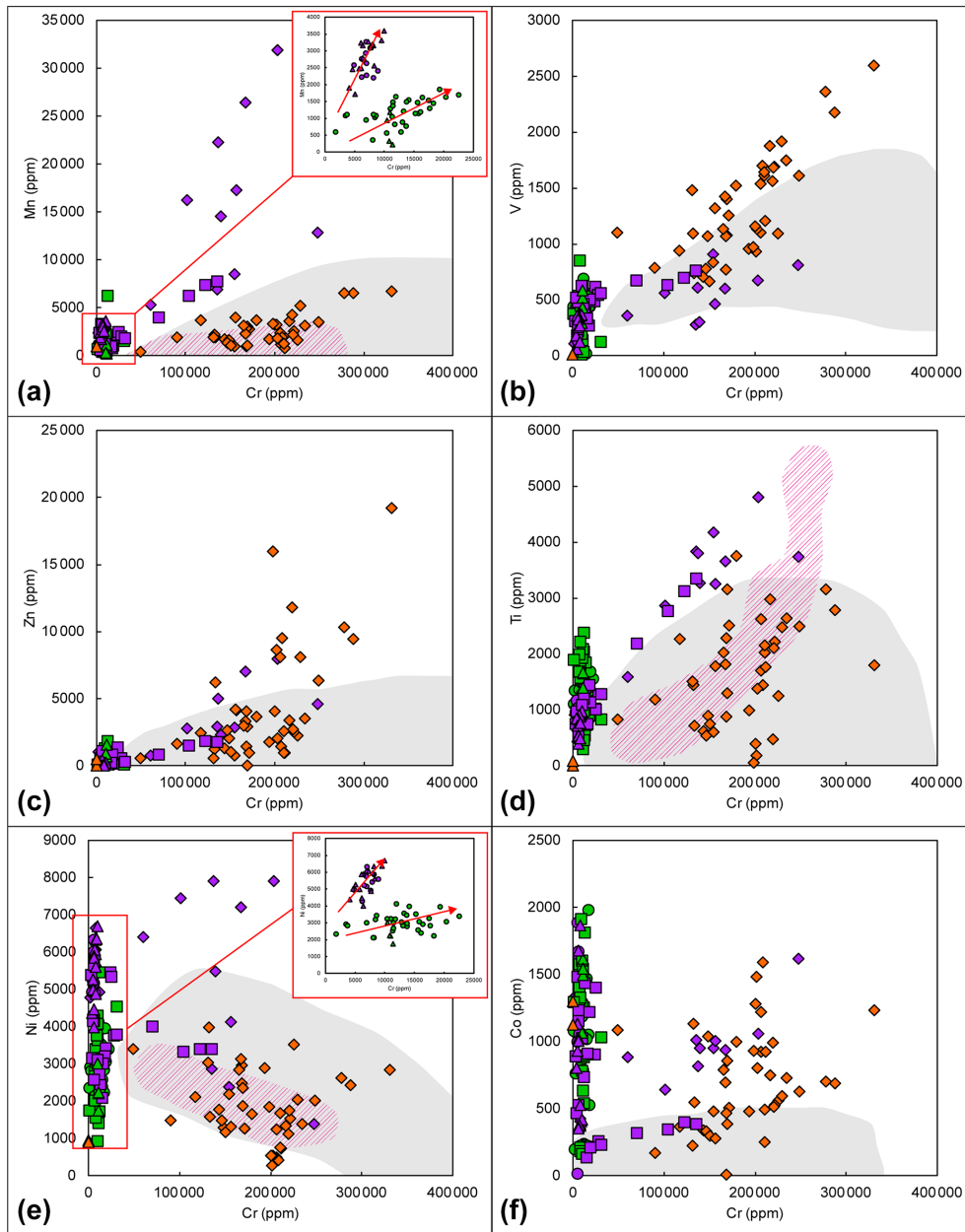
Figure 6. Correlation diagram of Cr vs. Mn, V, Zn, Ti, Ni, and Co, respectively (EMPA-WDS and LA-ICP-MS data). Values are in parts per million (ppm). Dashed pink areas refer to the composition of primary spinel from the Voltri Massif (mainly Erro-Tobbio primary spinels; Rampone et al., 2005; Piccardo and Visser, 2007; Borghini et al., 2007; Padovano et al., 2015); gray fields refer to the composition of ultramafic spinel worldwide (see Barnes and Roeder, 2001, and references therein). Enlarged boxes of **(a)** and **(e)** show the different compositional trend of the SSMs in the massive serpentinites and in the foliated serpentines. For the legend of symbols please refer to Fig. 2.

Mn, Zn, Co, and Ni, released after the breakdown of olivine, are incompatible with serpentine mineral structure and can be transported by the hydrothermal solution involved in serpentinization (Singh and Singh, 2013) and later incorporated in spinel crystal structure. SSM porphyroclasts in the VM massive serpentinites are richer in Ni than porphyroclasts in the partially serpentinized peridotites (see Fig. 6). This has been observed also in other geological context, and

it has been noted that Ni incorporation within chromite may be complicated by crystal–chemical effects and that Ni is more stable in magnetite due to the inverse spinel cation distribution (Hodel et al, 2017; Beckett-Brown and Mcdonald, 2018).

In general, compared to other ultramafic massifs worldwide, the relative abundance of Ni, Zn, and Co in the studied magnetites can also be explained by the low concentrations
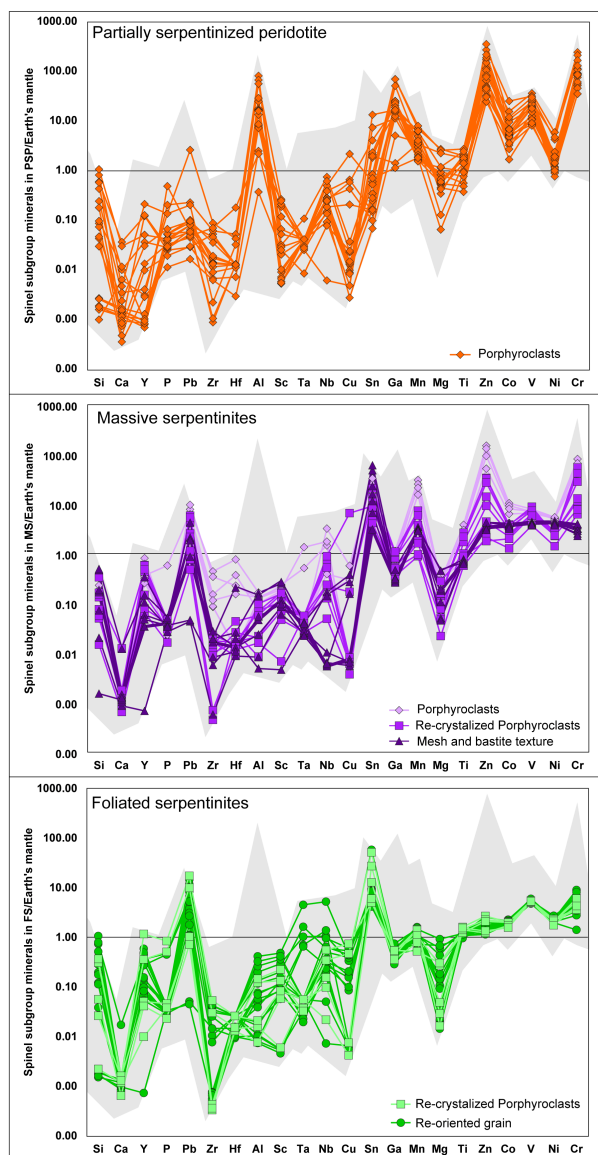
Figure 7. Multi-element variation diagrams of the analyzed SSMs after in situ laser ablation analysis (LA-ICP-MS data). The values have been normalized to the Earth's mantle average composition (Palme and O'Neill, 2014). Diamonds represent porphyroclast analyses, squares re-crystallized porphyroclasts, circles re-oriented magnetite, and triangles magnetite within pseudomorphic serpentine textures. The shaded gray area marks the sum of the ranges of the three different lithologies. The 22 trace elements are plotted in order of increasing compatibility into magnetite, as suggested by Dare et al. (2014).

Table 2. Accuracy by class of rock when all the 45 chemical elements are involved in the classification process. The last line reports the weighted averaged values of the true/false positive rate and the precision (FS – foliated serpentinites; PSP – partially serpentinized peridotites; MS – massive serpentinites).

True positive rate	False positive rate	Precision	Class
1.000	0.050	0.920	FS
1.000	0.000	1.000	PSP
0.905	0.000	1.000	MS
0.968	0.018	0.971	weighted averaged

Table 3. Confusion matrix related to the results obtained with a random forest classifier for classifying the rock type. All the 45 chemical elements are involved in the classification process (FS – foliated serpentinites; PSP – partially serpentinized peridotites; MS – massive serpentinites).

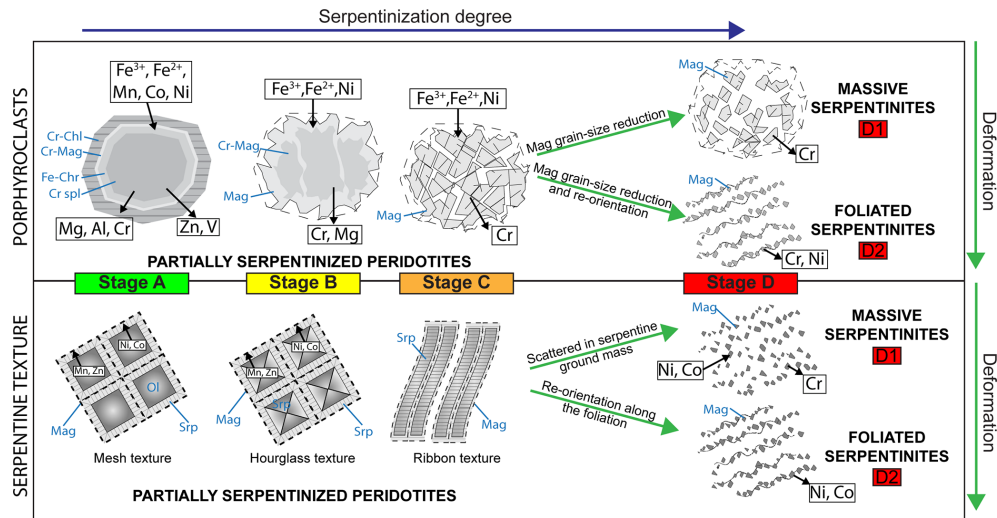|	FS	PSP	MS	Classified as
Actual type	23	0	0	FS
	0	19	0	PSP
	2	0	19	MS

stage reactions with serpentine or Mg- and Si-rich fluids, as suggested by Gonzalez-Jimenez et al. (2009).

The significant amount of Cr (~ 0.05 apfu) in bastite-hosted magnetite, regardless of the rock in which they occur, might be correlated with the high Cr content of pyroxenes that are, among silicates, the main Cr-bearing minerals (with enstatites reaching up to 13 000 ppm in Cr; Fornasaro et al., 2019).

It should be noted that the relatively high Al contents in some SSM crystals in the serpentine textures can be due to the presence of chlorite, which is intimately associated with antigorite in pseudomorphic and non-pseudomorphic textures (see Fornasaro et al., 2019).

5.3 Relationships between SSM composition and lithologic features: a data mining approach

In this work we present the first application of a machine learning approach (more precisely, using the software Weka 3.8.0; Frank et al., 2016) for evaluating the relationships among the compositional variations of SSMs, in relation to different textures and microstructures, and various degrees of serpentinization and deformation (lithotype). We checked the possibility of determining the host rock type and/or microstructure, starting from the quantitative knowledge of a set of chemical elements observed in SSMs. Machine learning algorithms are becoming increasingly used, and they are gaining popularity in an increasing variety of scientific disci-

of sulfide (Ni-sulfides) in our samples. A high Zn content in Cr-spinel core is common in metamorphosed ultramafic rocks (e.g., Barnes, 2000; Saumur et al., 2013). Compositional variations between cores and rims suggest that Zn behaves like Mg and is released from Cr-spinel during initial-

Figure 8. Sketch of SSM microstructure evolution. Stage A: development of mesh texture during the early oceanic serpentinization of peridotite. Stage B: first stage of Al-spinel substitution by Cr-magnetite, with intergrowth of serpentine minerals, and the progressive evolution of pseudomorphic texture (hourglass), triggered by the ongoing oceanic alteration. Stage C: complete replacement of Cr-magnetite by magnetite and development of ribbon texture during the ongoing oceanic serpentinization of the mantle rocks. Stage D1: grain-size reduction of magnetite in massive serpentinites. Stage D2: grain-size reduction and re-orientation of magnetite along the foliation in foliated serpentinites during the subduction and exhumation events.

Table 4. Accuracy by class of microstructure when all the 45 chemical elements are involved in the classification process. The last line reports the weighted averaged values of the true/false positive rate and the precision (A – SSM porphyroclasts; B – SSMs within pseudomorphic and non-pseudomorphic textures; C – re-oriented SSMs).

| True positive rate	False positive rate	Precision	Class
0.920	0.053	0.920	A
0.857	0.036	0.750	B
0.968	0.000	1.000	C
0.937	0.025	0.940	weighted averaged

Table 6. Accuracy by class of rock when a set of only eight chemical elements are involved in the classification process. The last line reports the weighted averaged values of the true/false positive rate and the precision (FS – foliated serpentinites; PSP – partially serpentinized peridotites; MS – massive serpentinites).

True positive rate	False positive rate	Precision	Class
1.000	0.050	0.920	FS
0.947	0.000	1.000	PSP
0.905	0.024	0.950	MS
0.952	0.026	0.954	weighted averaged

Table 5. Confusion matrix related to the results obtained with a random forest classifier for classifying the microstructure type. All the 45 chemical elements are involved in the classification process (A – SSM porphyroclasts; B – SSMs within pseudomorphic and non-pseudomorphic textures; C – re-oriented SSMs).

	A	B	C	Classified as
Actual type	23	2	0	A
	1	6	0	B
	1	0	30	C

plines as they are reputedly yielding reliable results. For our research, we used Weka 3.8.0 software, which is a powerful

open-access software including a large collection of machine learning algorithms. We tested several classifiers provided by Weka, and eventually we selected the random forest algorithm as the one which achieved the most accurate prediction for our data (detailed information on random forest classifiers can be found in Breiman, 2001). The achieved results clearly show that the classifier can produce a correct classification with a weighted averaged accuracy larger than 93 %, thus proving that the chemical composition of the SSMs is strongly affected by the type of rock as well as by texture and microstructure.

At first, the classifier was fed with the quantitative values related to the 45 elements (Li, Na, Cr, Mg, Al, Si, P, K, Ca, Sc, Ti, V, Mn, Co, Ni, Cu, Zn, Ga, Rb, Sr, Y, Zr, Nb, Sn, Cs,
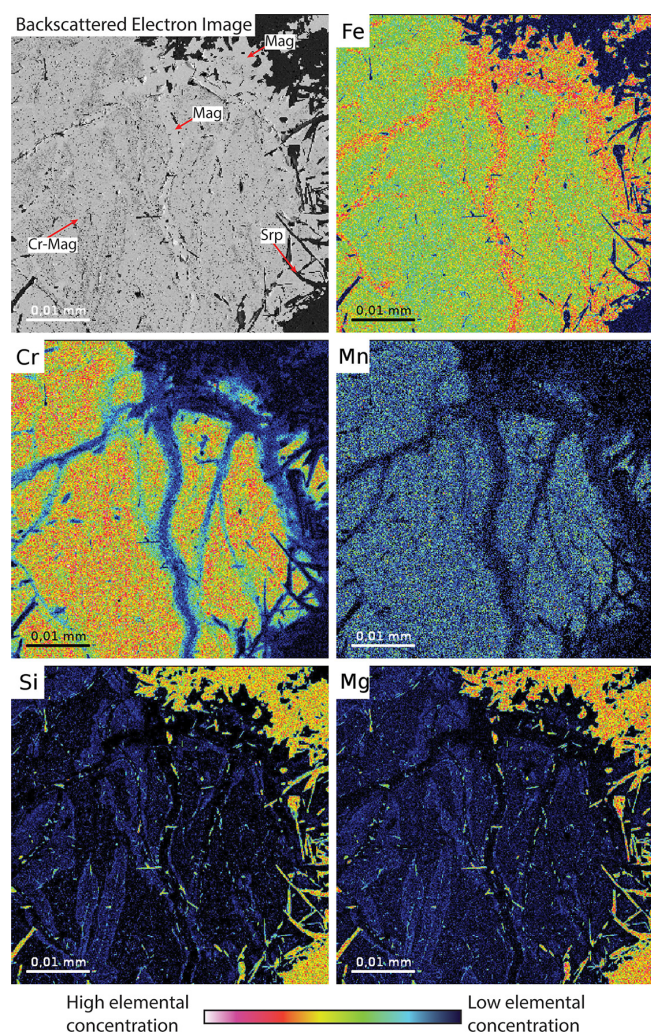
Figure 9. WDS compositional maps of Fe, Cr, Mn, Si, and Mg in a porphyroclast, showing the complete removal of chromium during chromian-spinel partial replacement by secondary magnetite along edges and microfractures.

Table 7. Confusion matrix related to the results obtained with a random forest classifier for classifying the rock type. Only eight chemical elements are involved in the classification process (FS – foliated serpentinites; PSP – partially serpentinized peridotites; MS – massive serpentinites).

	FS	PSP	MS	Classified as
Actual type	23	0	0	FS
	0	18	1	PSP
	2	0	19	MS

Ba, La, Ce, Pr, Nd, Sm, Eu, Gd, Tb, Dy, Ho, Er, Tm, Yb, Lu, Hf, Ta, Pb, Th, U) analyzed in SSMs grouped both for type of rock and microstructure (Tables 2–5). The performance of classifiers can be easily evaluated by means of confusion matrix (Table 3, sometimes named error matrix), a square

Table 8. Accuracy by class of microstructure when only eight chemical elements are involved in the classification process. The last line reports the weighted averaged values of the true/false positive rate and the precision (A – SSM porphyroclasts; B – SSMs within pseudomorphic and non-pseudomorphic textures; C – re-oriented SSMs).

True positive rate	False positive rate	Precision	Class
0.880	0.026	0.957	A
0.857	0.036	0.750	B
1.000	0.031	0.969	C
0.937	0.030	0.940	weighted averaged

Table 9. Confusion matrix related to the results obtained with a random forest classifier for classifying the microstructure type. Only eight chemical elements are involved in the classification process (A – SSM porphyroclasts; B – SSMs within pseudomorphic and non-pseudomorphic textures; C – re-oriented SSMs).

	A	B	C	Classified as
Actual type	22	2	1	A
	1	6	0	B
	0	0	31	C

matrix that shows counts from predicted and actual values. All correct predictions are located on the diagonal of the matrix. Conversely, erroneous predictions are out the diagonal; specifically, false positives are below the diagonal and false negatives above the diagonal (Bonaccorso, 2022). Concerning the possible classification by the rock type, the confusion matrix obtained with a random forest classifier (Table 3) highlights that only two samples were incorrectly classified as MS instead FS, with a precision of 97 %. On the other hand, the confusion matrix obtained for classifying the microstructure type gives a good classification with only two incorrectly classified samples, with a precision of 94 % (Table 5).

Finally, a reduced set of chemical elements, selected with "best first" method provided by the software (i.e., Na, Mg, Co, Ni, Zn, Ga, Rb, and Th) was employed to perform the classification again: the results (reported in Tables 6–9) highlight the good performance of the random forest classifier, which allows achieving accuracies only slightly smaller than those obtained when all the 45 elements were taken into account.

6 Conclusions

In this study we investigated the mineralogy and the mineral chemistry of SSMs in different ultramafic rocks (i.e.,

partially serpentinized peridotites, massive serpentinites, and foliated serpentinites) from the Voltri Massif $HP-LT$ metaophiolites (Ligurian Alps). We focused on variations of the SSM composition in relation to different textures, microstructures, and the various degree of serpentinization and deformation of these metamorphic ultramafites.

In the selected rocks, the SSMs occur within several textural and microstructural features that can be grouped into three main classes: (i) SSM porphyroclasts with various degree of recrystallization, scattered within partially serpentinized peridotite and massive serpentinite; (ii) SSMs within pseudomorphic and non-pseudomorphic serpentine textures within partially serpentinized peridotite and massive serpentinite; and (iii) SSMs re-oriented along the foliation within foliated serpentinites.

The results highlighted a significant variation in the contents of trace and ultratrace elements in SSMs during the evolution from Cr-spinel porphyroclast occurring in partially serpentinized peridotites to the various generations of magnetite (Fig. 2). This chemical variation may be related to the serpentinization and deformation evolution of the studied ultramafic rocks. The breakdown of olivine during serpentinization causes the release of Mn, Zn, Ni, and Co, which can be trapped within the lattice of chromian spinel. As serpentinization and the following deformation progress, Cr, Ni, and Co concentrations progressively decrease.

Our findings are confirmed by an innovative indirect statistical method performed by the machine learning approach. The method clearly shows that the classifier can produce a correct classification with a weighted averaged accuracy larger than 93 %, thus proving that the composition variation in SSMs is strongly affected by both the rock type and the microstructure. On the one hand, this further highlights a strong correlation between a (possibly selected) set of elements and the textural and microstructural features; the possibility to achieve a good classification starting from a limited set of chemical elements permits us to reduce the overall cost of the analysis and allows researchers to focus on other possibly crucial points of the investigation.

It should be noted that, compared to other ultramafic SSMs, the relative abundance of Ni, Zn, and Co in magnetite of VM can also be linked to the low concentrations of sulfide in these rocks.

At a general scale, the trace and ultratrace variability in SSMs is primarily related to the petrologic and tectonic evolution but at a local scale. On the other hand, the mineralogical, lithological, structural, and textural features correlated to the degree of serpentinization and/or deformation significantly influence their distribution and concentration in trace and ultratrace elements.

These variations may also have significant environmental implications since some of these trace elements are potentially toxic elements which can be released to soil and circulating water, depending on the host minerals and their stability during weathering and pedogenic processes. Furthermore, this data might be used for the evaluation of the pedogeochemical background for naturally occurring contaminants.

References

Abre, P., Cingolani, C., Zimmermann, U., and Cairncross, B.: Detrital chromian spinels from Upper Ordovician deposits in the Precordillera terrane, Argentina: a mafic crust input, J. S. Am. Earth Sci., 28, 407–418, https://doi.org/10.1016/j.jsames.2009.04.005, 2009

Barnes, S. J.: Chromite in komatiites, I. Magmatic controls on crystallization and composition, J. Petrol., 39, 1689–1720, https://doi.org/10.1093/petroj/39.10.1689, 1998.

Barnes, S. J.: Chromite in komatiites, II modification during Greenschist to mid-amphibolite facies metamorphism, J. Petrol., 41, 387–409, https://doi.org/10.1093/petrology/41.3.387, 2000.

Barnes, S. J. and Roeder, P. L.: The range of spinel compositions in terrestrial mafic and ultramafic rocks, J. Petrol., 42, 2279–2302, https://doi.org/10.1093/petrology/42.12.2279, 2001.

Beckett-Brown, C. E. and McDonald, A. M.: The Crystal-chemistry of Ni-bearing Spinel-group Minerals: Chemical, Geological, and Exploration Implications, Can. Mineral., 56, 77–94, https://doi.org/10.3749/canmin.1700054, 2018.

Bliss, N. W. and MacLean, W. H.: The paragenesis of zoned chromite from central Manitoba, in: Chromium: its Physicochemical Behavior and Petrologic Significance, 973–990, ISBN 0-08-019954-2, 1975.

Bonaccorso, G.: Machine Learning Algorithms: Popular algorithms for data science and machine learning, Second Edition, Packt Publishing, ISBN: 9781789347999, 2022.

Borghini, G., Rampone, E., Crispini, L., De Ferrari, R., and Godard, M.: Origin and emplacement of ultramafic–mafic intrusions in the Erro-Tobbio mantle peridotite (Ligurian Alps, Italy), Lithos, 94, 210–229, https://doi.org/10.1016/j.lithos.2006.06.014, 2007.

Bosi, F., Biagioni, C., and Pasero, M.: Nomenclature and classification of the spinel supergrop, Europ. J. Mineral., 31, 183–192, 2019.

Breiman, L.: Random Forests, Mach. Learn., 45, 5–32, 2001

Cannaò, E., Scambelluri, M., Agostini, S., Tonarini, S., and Godard, M.: Linking serpentinite geochemistry with tectonic evolution at the subduction plate-interface: The Voltri Massif case study (Ligurian Western Alps, Italy), Geochim. Cosmochim. Ac., 190, 115–133, https://doi.org/10.1016/j.gca.2016.06.034, 2016.

Capponi G., Crispini L., Federico L., and Malatesta C.: Geology of the Eastern Ligurian Alps: a review of the tectonic units, Ital. J. Geosci., 135, 157–169, https://doi.org/10.3301/IJG.2015.06, 2016.

Capponi, G. and Crispini, L.: Structural and metamorphic signature of alpine tectonics in the Voltri Massif (Ligurian Alps, northwestern Italy), Eclogae. Geol. Helv., 95, 31–32, 2002.

Capponi, G., Crispini, L., Federico, L., Cabella, R., Faccini, F., Ferraris, F., Firpo, M., Marescotti, P., Piazza, M., Scambelluri, M., Vetuschi Zuccolini, M., and Roccati, A.: Note illustrative al Foglio 212 "Spigno Monferrato" della Carta Geologica Regionale della Liguria, Regione Liguria, Dipartimento Ambiente, Genova, Italy, 144 pp., 2013.

Chen, F., Deng, J., Wang, Q., Huizenga, J. M., Li, G., and Gu, Y.: LA-ICP-MS trace element analysis of magnetite and pyrite from the Hetaoping Fe-Zn-Pb skarn deposit in Baoshan block, SW China: Implications for ore-forming processes, Ore. Geol. Rev., 117, 103309, https://doi.org/10.1016/j.oregeorev.2020.103309, 2020.

Christofides, G., Thimiatis, G., Koroneos, A., Sklavounos, S. N. S., and Eleftheriadis, G.: Mineralogy and chemistry of Cr-chlorites associated with chromites from Vavdos and Vasilika ophiolite complexes (Chalikidiki, Macedonia, N. Greece), Chem. Erde, 54, 151–166, 1994.

Colás, V., González-Jiménez, J. M., Griffin, W. L., Fanlo, I., Gervilla, F., O'Reilly, S. Y., and Proenza, J. A.: Fingerprints of metamorphism in chromite: new insights from minor and trace elements, Chem. Geol., 389, 137–152, https://doi.org/10.1016/j.chemgeo.2014.10.001, 2014.

Comodi, P., Boffa Ballaran, T., Zanazzi, P. F., Capalbo, C., Zanetti, A., and Nazzareni, S.: The effect of oxo-component on the high-pressure behavior of amphiboles, Am. Mineral., 95, 1042–1051, https://doi.org/10.2138/am.2010.3429, 2010.

Dare, S. A., Barnes, S. J., Beaudoin, G., Méric, J., Boutroy, E., and Potvin-Doucet, C.: Trace elements in magnetite as petrogenetic indicators, Miner. Deposita, 49, 785–796, https://doi.org/10.1007/s00126-014-0529-0, 2014.

Deditius, A. P., Reich, M., Simon, A. C., Suvorova, A., Knipping, J., Roberts, M. P., and Saunders, M.: Nanogeochemistry of hydrothermal magnetite, Contrib. Mineral. Petrol., 173, 1–20, https://doi.org/10.1007/s00410-018-1474-1, 2018.

Descamps, E. C. T., Abbé, J.-B., Pignol, D., and Lefèvre, C. T.: Controlled biomineralization of magnetite in bacteria, in: Iron oxides. From nature to applications, edited by: Faivre, D., Wiley-VCH Verlag GmbH and Co. KGaA, Weinheim, Germany, 99–116, ISBN 978-3-527-33882-5, 2016.

Diella, V., Ferrario, A., and Rossetti, P.: The magnetite ore deposits of the southern Aosta valley: chromitite transformed during an Alpine metamorphic event, Ofioliti, 19, 247–256, 1994.

Droop, G. T. R.: A general equation for estimating Fe_3^+ concentrations in ferromagnesian silicates and oxides from microprobe analyses, using stoichiometric criteria, Mineral. Mag., 51, 431–435, 1987.

Duivenvoorden, L. J., Roberts, D. T., and Tucker, G. M.: Serpentine geology links to water quality and heavy metals in sediments of a stream system in central Queensland, Austr. Environ. Earth. Sci., 76, 1–14, https://doi.org/10.1007/s12665-017-6615-8, 2017.

Dupuis, C. and Beaudoin, G.: Discriminant diagrams for iron oxide trace element fingerprinting of mineral deposit types, Miner. Deposita, 46, 319–335, https://doi.org/10.1007/s00126-011-0334-y, 2011.

Evans, B. and Frost, R. B.: Chrome spinel in progressive metamorphism: a preliminary analysis, Geochim. Cosmochim. Ac., 39, 959–972, 1975.

Federico, L., Crispini, L., Malatesta, C., Torchio, S., and Capponi, G.: Geology of the Pontinvrea area (Ligurian Alps, Italy): structural setting of the contact between Montenotte and Voltri units, J. Maps, 11, 101–113, https://doi.org/10.1080/17445647.2014.945749, 2015.

Fontana, E., Panseri, M., and Tartarotti, P.: Oceanic relict textures in the Mount Avic serpentinites, Western Alps, Ofioliti, 33, 105–118, 2008.

Fornasaro, S., Comodi, P., Crispini, L., Malatesta, C., Zucchini, A., and Marescotti, P.: Potentially toxic elements distribution in the serpentinized and deformed ultramafic rocks from the Voltri Massif (NW, Italy), Period. Mineral., 88, 259–276, https://doi.org/10.2451/2019PM874, 2019.

Frank, E., Hall, M. A., and Witten, I. H.: The WEKA Workbench. Online Appendix for "Data Mining: Practical Machine Learning Tools and Techniques", Morgan Kaufmann, 4th Edn., ISBN 1-55860-552-5, 2016.

Gahlan, H. A. and Arai, S.: Genesis of peculiarly zoned Co, Zn and Mn-rich chromian spinel in serpentinite of Bou-Azzer ophiolite, Anti-Atlas, Morocco, J. Miner. Petrol. Sci., 102, 69–85, https://doi.org/10.2465/jmps.060212, 2007.

Gargiulo, M. F., Bjerg, E. A., and Mogessie, A.: Spinel group minerals in metamorphosed ultramafic rocks from Río de Las Tunas belt, Central Andes, Argentina, Geol. Acta, 11, 133–148, https://doi.org/10.1344/105.000001836, 2013.

Garuti, G., Proenza, J. A., and Zaccarini, F.: Distribution and mineralogy of platinum-group elements in altered chromitites of the Campo Formoso layered intrusion (Bahia State, Brazil): Control by magmatic and hydrothermal processes, Miner. Petrol., 89, 159–188, https://doi.org/10.1007/s00710-006-0141-9, 2007.

Gervilla, F., Padrón-Navarta, J. A., Kerestedjian, T., Sergeeva, I., González-Jiménez, J. M., and Fanlo, I.: Formation of ferrian chromite in podiform chromitites from the Golyamo Kamenyane serpentinite, Eastern Rhodopes, SE Bulgaria: a two-stage process, Contrib. Mineral. Petrol., 164, 643–657, https://doi.org/10.1007/s00410-012-0763-3, 2012.

Gonzalez-Jiménez, J. M., Kerestedjian, T., Fernández, J. A. P., and Linares, F. G.: Metamorphism on chromite ores from the Dobromirtsi ultramafic massif, Rhodope mountains (SE Bulgaria), Geol. Acta, 7, 413–429, https://doi.org/10.1344/104.000001447, 2009.

Grieco, G. and Merlini, A.: Chromite alteration processes within Vourinos ophiolite, Int. J. Earth Sci., 101, 1523–1533, https://doi.org/10.1007/s00531-011-0693-8, 2012.

Hodel, F., Macouin, M., Triantafyllou, A., Carlut, J., Berger, J., Rousse, S., and Trindade, R. I. F.: Unusual massive magnetite veins and highly altered Cr-spinels as relics of a Cl-rich acidic hydrothermal event in Neoproterozoic serpentinites (Bou Azzer ophiolite, Anti-Atlas, Morocco), Precambrian Res., 300, 151–167, https://doi.org/10.1016/j.precamres.2017.08.005, 2017.

Irvine, T. N.: Chromian spinel as a petrogenetic indicator: Part 2. Petrologic applications, Can. J. Earth Sci., 4, 71–103, 1967.

Kimball, K. L.: Effects of hydrothermal alteration on the composition of chromian spinels, Contrib. Mineral. Petrol., 105, 337–346, 1990.

King, R. J.: Minerals explained 40, The spinels, Geol. Today, 20, 194–200, 2004.

Marescotti, P., Comodi, P., Crispini, L., Gigli, L., Zucchini, A., and Fornasaro, S.: Potentially Toxic Elements in Ultramafic Soils: A Study from Metamorphic Ophiolites of the Voltri Massif (Western Alps, Italy), Minerals, 9, 502, https://doi.org/10.3390/min9080502, 2019.

Mellini, M., Rumori, C., and Viti, C.: Hydrothermally reset magmatic spinels in retrograde serpentinites: formation of "ferritchromit" rims and chlorite aureoles, Contrib. Mineral. Petrol., 149, 266–275, https://doi.org/10.1007/s00410-005-0654-y, 2005.

Merlini, A., Tartarotti, P., Grieco, G., Sansone, M., Rizzo, G., and Prosser, G.: Coupled ferritchromite and chromian-chlorite in mantle rocks: a comparison from circum-mediterranean ophiolites, Rend. Online Soc. Geol. It., 21, 305–307, 2012.

Messiga, B., Piccardo, G. B., and Ernst, W. G.: High pressure Eo-Alpine parageneses developed in magnesian metagabbros, Gruppo di Voltri, Western Liguria, Italy, Contrib. Mineral. Petrol., 83, 1–15, https://doi.org/10.1007/BF00373074, 1983.

Nadoll, P., Angerer, T., Mauk, J. L., French, D., and Walshe, J.: The chemistry of hydrothermal magnetite: A review, Ore Geol. Rev., 61, 1–32, https://doi.org/10.1016/j.oregeorev.2013.12.013, 2014.

Padovano, M., Piccardo, G. B., and Vissers, R. L.: Tectonic and magmatic evolution of the mantle lithosphere during the rifting stages of a fossil slow–ultraslow spreading basin: insights from the Erro–Tobbio peridotite (Voltri Massif, NW Italy), Geol. Soc. Lond. Spec. Publ., 413, 205–238, https://doi.org/10.1144/SP413.7, 2015.

Pagè, P. and Barnes, S. J.: Using trace elements in chromites to constrain the origin of podiform chromitites in the Thetford Mines ophiolite, Québec, Canada, Econ. Geol., 104, 997–1018, https://doi.org/10.2113/econgeo.104.7.997, 2009.

Palme, H. and O'Neill, H.: Cosmochemical estimates of mantle composition, Treat. Geochem., 2nd Edn., Elsevier, https://doi.org/10.1016/B978-0-08-095975-7.00201-1, 2014.

Peters, D., Pettke, T., John, T., and Scambelluri, M.: The role of brucite in water and element cycling during serpentinite subduction – Insights from Erro Tobbio (Liguria, Italy), Lithos, 360/361, 105431, https://doi.org/10.1016/j.lithos.2020.105431, 2020

Petrelli, M., Morgavi, D., Vetere, F., and Perugini, D.: Elemental imaging and petro-volcanological applications of an improved laser ablation inductively coupled quadrupole plasma mass spectrometry, Period. Mineral., 85, 25–39, https://doi.org/10.2451/2015PM0465, 2016.

Piccardo, G. B. and Vissers, R. L. M.: The pre-oceanic evolution of the Erro-Tobbio peridotite (Voltri Massif, Ligurian Alps, Italy), J. Geodyn., 43, 417–449, https://doi.org/10.1016/j.jog.2006.11.001, 2007.

Piccardo, G. B., Rampone, E., Romairone, A., Scambelluri, M., Tribuzio, R., and Beretta, C.: Evolution of the Ligurian Tethys: inference from petrology and geochemistry of the Ligurian Ophiolites, Period. Mineral., 70, 147–192, 2001.

Rampone, E., Romairone, A., Abouchami, W., Piccardo, G. B., and Hofmann, A. W.: Chronology, Petrology and Isotope Geochemistry of the Erro-Tobbio Peridotites (Ligurian Alps, Italy): Records of Late Palaeozoic Lithospheric Extension, J. Petrol., 46, 799–827, https://doi.org/10.1093/petrology/egi001, 2005.

Rollinson, H.: The geochemistry of mantle chromitites from the northern part of the Oman ophiolite: inferred parental melt compositions, Contrib. Mineral. Petr., 156, 273–288, https://doi.org/10.1007/s00410-008-0284-2, 2008.

Romero-Freire, A., Olmedo-Cobo, J., and Gómez-Zotano, J.: Elemental concentration in serpentinitic soils over ultramafic bedrock in Sierra Bermeja (Southern Spain), Minerals, 8, 447, https://doi.org/10.3390/min8100447, 2018.

Saumur, B. M. and Hattori, K.: Zoned Cr-spinel and ferritchromite alteration in forearc mantle serpentinites of the Rio San Juan Complex, Dominican Republic, Mineral. Mag., 77, 117–136, https://doi.org/10.1180/minmag.2013.077.1.11, 2013.

Scambelluri, M., Strating, E. H., Piccardo, G. B., Vissers, R. L. M., and Rampone, E.: Alpine olivine-and titanian clinohumite-bearing assemblages in the Erro-Tobbio peridotite (Voltri Massif, NW Italy), J. Metamor. Geol., 9, 79–91, https://doi.org/10.1111/j.1525-1314.1991.tb00505.x, 1991.

Scarsi, M., Malatesta, C., and Fornasaro, S.: Lawsonite-bearing eclogite from a tectonic mélange in the Ligurian Alps: new constraints for the subduction plate-interface evolution, Geol. Mag., 155, 280–297, https://doi.org/10.1017/S0016756817000395, 2018.

Singh, A. K. and Singh, R. B.: Genetic implications of Zn- and Mn-rich Cr-spinels in serpentinites of the Tidding Suture Zone, eastern Himalaya, NE India. Geol. J., 48, 22–38, https://doi.org/10.1002/gj.2428, 2013.

Teixeira, R. J., Neiva, A. M., and Gomes, M. E.: Chromian spinels and magnetite of serpentinites, steatitic rocks, tremolite asbestos and chloritites from Bragança massif, northeastern Portugal, Period. Mineral., 81, https://doi.org/10.2451/2012PM0014, 2012.

Warr, L. N.: IMA-CNMNC approved minerals symbols, Mineral. Mag., 85, 291–320, http://https://doi.org/10.1180/mgm.2021.43, 2021.